



Deposited via The University of Leeds.

White Rose Research Online URL for this paper:

<https://eprints.whiterose.ac.uk/id/eprint/179425/>

Version: Accepted Version

---

**Article:**

Mangan, TP, Douglas, KM, Lade, RE et al. (2021) Kinetic Study of the Reactions of AlO with H<sub>2</sub>O and H<sub>2</sub>; Precursors to Stellar Dust Formation. ACS Earth and Space Chemistry, 5 (12). pp. 3385-3395. ISSN: 2472-3452

<https://doi.org/10.1021/acsearthspacechem.1c00225>

---

**Reuse**

Items deposited in White Rose Research Online are protected by copyright, with all rights reserved unless indicated otherwise. They may be downloaded and/or printed for private study, or other acts as permitted by national copyright laws. The publisher or other rights holders may allow further reproduction and re-use of the full text version. This is indicated by the licence information on the White Rose Research Online record for the item.

**Takedown**

If you consider content in White Rose Research Online to be in breach of UK law, please notify us by emailing [eprints@whiterose.ac.uk](mailto:eprints@whiterose.ac.uk) including the URL of the record and the reason for the withdrawal request.

1 **Kinetic study of the reactions of AlO with H<sub>2</sub>O and H<sub>2</sub>; precursors to stellar dust**  
2 **formation**

3

4

5 Thomas P. Mangan<sup>1</sup>, Kevin M. Douglas<sup>1</sup>, Rachel E. Lade<sup>1</sup>, David Gobrecht<sup>2</sup>, Leen Decin<sup>1, 2</sup>  
6 and John M. C. Plane\*<sup>1</sup>

7

8

9 <sup>1</sup> School of Chemistry, University of Leeds, Woodhouse Lane, Leeds LS2 9JT, UK.

10 <sup>2</sup> Department of Physics and Astronomy, Institute of Astronomy, KU Leuven,  
11 Celestijnenlaan 200 D, B-3001 Leuven (Heverlee), Belgium.

12

13

14 \*corresponding author. Email: [j.m.c.plane@leeds.ac.uk](mailto:j.m.c.plane@leeds.ac.uk)

15

16

17

18

19 Keywords: aluminium oxide reactions; laser-based kinetic technique; RRKM theory; Master  
20 equation analysis; electronic structure theory; AGB stars; stellar outflow chemistry; alumina  
21 dust formation

22

23

24 **Abstract**

25 AlO is relatively abundant around oxygen-rich Asymptotic Giant Branch (AGB) stars, where  
26 it can react with abundant gas-phase species such as H<sub>2</sub> and H<sub>2</sub>O to form AlOH. These Al-  
27 containing species are the likely precursors of refractory alumina nano-particles, which may  
28 provide the nuclei for dust formation. In the present study, the kinetics of these AlO reactions  
29 were measured from 295 - 780 K using the pulsed laser photolysis of Al(C<sub>5</sub>H<sub>7</sub>O<sub>2</sub>)<sub>3</sub>, with time-  
30 resolved laser induced fluorescence detection of AlO. The experimental results were  
31 interpreted using quantum chemistry calculations and a Master Equation solver for reactions  
32 with multiple energy wells. For the recombination reaction AlO + H<sub>2</sub>O (+ N<sub>2</sub>) → Al(OH)<sub>2</sub>,  
33  $\log_{10}(k_{\text{rec},0} / \text{cm}^6 \text{ molecule}^{-2} \text{ s}^{-1}) = -32.9185 + 8.80276 \log_{10}(T) - 2.4723(\log_{10}(T))^2$ ;  $\log_{10}(k_{\text{rec},\infty}$   
34  $/ \text{cm}^3 \text{ molecule}^{-1} \text{ s}^{-1}) = -19.4686 + 7.62037 \log_{10}(T) - 1.47214(\log_{10}(T))^2$ ;  $F_c = 0.28$   
35 (uncertainty  $\pm 13\%$  from 295 – 760 K). For the bimolecular reactions,  $k(\text{AlO} + \text{H}_2\text{O} \rightarrow \text{AlOH}$   
36  $+ \text{OH}) = (3.89 \pm 0.47) \times 10^{-10} \exp(-(1295 \pm 150)/T)$  and  $k(\text{AlO} + \text{H}_2 \rightarrow \text{AlOH} + \text{H}) = (5.37 \pm 0.52)$   
37  $\times 10^{-13} (T/300)^{(2.77 \pm 0.19)} \exp(-(2190 \pm 110)/T) \text{ cm}^3 \text{ molecule}^{-1} \text{ s}^{-1}$ . Rate coefficients for Al + H<sub>2</sub>O  
38 → AlOH + H, AlOH + H → AlO + H<sub>2</sub> or Al + H<sub>2</sub>O, and the absorption cross sections of AlOH  
39 and AlO, were calculated theoretically. Al chemistry around an O-rich AGB star was then  
40 investigated using a  $\beta$ -trajectory model, which predicts that AlOH is the major gas-phase Al  
41 species beyond two stellar radii, and shows that the relative AlO abundance is very sensitive  
42 to the AlOH photolysis rate.

43

44

## 45 Introduction

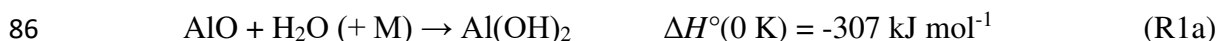
46 Asymptotic Giant Branch (AGB) stars are evolved stars experiencing significant mass loss at  
47 the end of their lifecycle. Within the CircumStellar Envelope (CSE) around an AGB star, gas-  
48 phase chemistry produces thermally stable molecules which aggregate and condense into dust  
49 particles as the gas cools, forming an optically thick shell.<sup>1</sup> The release of molecules and dust  
50 formation in the CSEs around AGB stars are a major source of dust grains in the universe.<sup>2</sup>

51 A range of candidates has been proposed for the primary initial dust grains around oxygen-rich  
52 AGB stars (i.e.  $C/O < 1$ ), including metal titanates, metal silicates, SiO and Al<sub>2</sub>O<sub>3</sub> (alumina).<sup>3</sup>  
53 <sup>4</sup> Many infra-red (IR) spectra of O-rich CSEs suggest that O-rich dust such as silicates, and  
54 especially alumina, are likely candidates for the initial dust grains.<sup>4</sup> Alumina is particularly  
55 favoured as an initial dust seed in the inner wind of O-rich AGB stars due to its refractory  
56 nature and high condensation temperature (around 1400 K).<sup>5</sup> A broad emission band at 11  $\mu\text{m}$   
57 in the IR spectra of many O-rich AGB stars is widely thought to come from amorphous Al<sub>2</sub>O<sub>3</sub>.<sup>6</sup>  
58 <sup>7</sup> Begemann *et al.* <sup>8</sup> determined the optical constants of alumina particles and showed that a  
59 feature at 13  $\mu\text{m}$  might arise from crystalline  $\alpha$ -Al<sub>2</sub>O<sub>3</sub> (corundum), although Posch *et al.* <sup>9</sup>  
60 suggested MgAl<sub>2</sub>O<sub>4</sub> (spinel) as a more likely carrier. Subsequently, Sloan *et al.* <sup>10</sup> used  
61 correlations between IR spectra to argue that the 13  $\mu\text{m}$  band arises from crystalline Al<sub>2</sub>O<sub>3</sub>.  
62 When modelling the CSEs of a group of 37 AGB stars in the Large Magellanic Cloud, Jones  
63 *et al.* <sup>11</sup> found that an appreciable fractional abundance of alumina in dust (up to 50%) improved  
64 the fitting of IR spectra. For AGB stars S Ori and R Cnc, Karovicova *et al.* <sup>5</sup> were able to  
65 describe the observed spectra with a pure alumina dust shell.

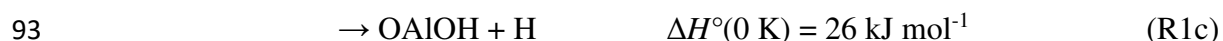
66 A range of Al-containing species has been observed around AGB stars, with AlO and AlOH  
67 the most abundant.<sup>7, 12, 13, 14</sup> AlO has also been detected in the CSE of the young, massive star  
68 Orion Source I.<sup>15</sup> These relatively abundant Al species are thought to be the direct precursors  
69 to alumina dust, with Gobrecht *et al.* <sup>16</sup> proposing that AlO undergoes dimerization to (AlO)<sub>2</sub>,  
70 which is then oxidized to Al<sub>2</sub>O<sub>3</sub>. The Al<sub>2</sub>O<sub>3</sub> then itself dimerizes before clustering further and  
71 condensing to form dust grains. Other reaction pathways to alumina may be possible, including  
72 reactions involving AlO, AlOH and Al(OH)<sub>2</sub> with other gas-phase species.<sup>17</sup>

73 Decin *et al.* <sup>14</sup> found that the variable chemistry of AGB stars leads to differences in the  
74 fractional abundances of AlO and AlOH, with both species apparent at distances from the star  
75 both before and after dust condensation occurs. For example, AlOH is more readily detected  
76 than AlO in the CSE of high mass-loss Mira-type O-rich star IK Tau, while conversely AlO is  
77 approximately 70 times more abundant in the CSE of the low mass-loss rate semi-regular O-  
78 rich AGB star R Dor. In the O-rich red supergiant VY CMa, AlOH was found to be 17 times  
79 more abundant than AlO.<sup>12</sup> Understanding the gas-phase chemistry between AlO and AlOH in  
80 CSEs (where temperatures in the dust formation region are around 500 – 2000 K) is crucial to  
81 understanding the variable chemistry observed from star to star and in understanding the initial  
82 steps of how dust forms around AGB stars.

83 H<sub>2</sub>O is one of the more abundant reactive species around O-rich AGB stars; e.g. the relative  
84 abundance of H<sub>2</sub>O to H<sub>2</sub> at IK Tau is  $6.6 \times 10^{-5}$ .<sup>18</sup> H<sub>2</sub>O could react with AlO in a termolecular  
85 recombination reaction:



87 where M is the bath gas (H<sub>2</sub> in the case of stellar chemistry). Reactions of this type should  
88 become slower with increasing temperature, and should be pressure-dependent. Therefore, in  
89 the relatively low pressure and high temperature environment close to an AGB star it may be  
90 a minor removal pathway for AlO, while bimolecular reaction channels may become more  
91 important:



95 Depending on the specific AGB star,  $\text{H}_2$  is 4 - 10 orders of magnitude more abundant than any  
 96 other species, and so could provide another possible pathway to AlOH formation via R2a:



99 The reactions



102 and



105 take place on the same potential energy surface (PES) as R2, and are likely to be important in  
 106 outflow chemistry because of the relatively large abundances of  $\text{H}_2\text{O}$  and  $\text{H}$ . The enthalpy  
 107 changes (at 0 K) listed above for these reactions are calculated at the G4 level of theory<sup>19, 20</sup>  
 108 (see the Discussion). All of these bimolecular reaction channels (apart from R1d which is  
 109 significantly endothermic compared to the other channels of R1) could potentially influence  
 110 the gas-phase abundances of AlO and AlOH around AGB stars, and hence the rate of alumina  
 111 dust formation in their CSEs.

112 Another reason for studying reaction 1 concerns the chemistry of Al which ablates from cosmic  
 113 dust entering planetary atmospheres.<sup>21, 22</sup> Al atoms react rapidly with  $\text{O}_2$  to form AlO,<sup>23</sup> which  
 114 can then recombine with  $\text{H}_2\text{O}$  at the comparatively lower temperatures ( $< 300 \text{ K}$ ) and higher  
 115 pressures ( $\sim 10^{-6} \text{ bar}$ ) typical of the atmospheric region in which ablation occurs.<sup>24</sup> In our  
 116 recent study of the chemistry of meteor-ablated Al in the Earth's upper mesosphere, we used  
 117 quantum calculations to show that AlOH may have a large photolysis cross section below 260  
 118 nm, and this would significantly change the AlO/AlOH ratio.<sup>22</sup> AlOH photolysis is also likely  
 119 to be important in the inner region of a stellar outflow, before the stellar radiation is obscured  
 120 by dust formation.

121 To the best of our knowledge, the reaction kinetics of AlO with  $\text{H}_2\text{O}$  has not been studied  
 122 previously, and only an upper limit for AlO +  $\text{H}_2$  of  $5 \times 10^{-14} \text{ cm}^3 \text{ molecule}^{-1} \text{ s}^{-1}$  has been  
 123 reported at 298 K.<sup>25</sup> The reaction of Al with  $\text{H}_2\text{O}$  has been studied from 298-1174 K,<sup>26</sup> though  
 124 the products were not identified. There do not appear to be any experimental studies of the  
 125 reaction between AlOH and H.

126 In the present study we report kinetic measurements of R1 and R2 at temperatures up to 780  
 127 K. A combination of electronic structure calculations and Rice-Ramsperger-Kassel-Markus  
 128 (RRKM) theory is then used to extrapolate the experimental results over the full temperature  
 129 range (150 – 2000 K) pertinent to both planetary atmospheres and dust formation around AGB  
 130 stars (500 - 2000 K), as well as predicting the reaction products. Reactions R3 and R4 are  
 131 explored in the same way. In the final part of the Discussion we explore the impact of these  
 132 reactions, together with AlOH photolysis, on the ratio of AlO to AlOH around two examples  
 133 of AGB stars.

134

## 135 **Experimental**

136 Reactions R1 and R2 were studied using the pulsed laser photolysis-laser induced fluorescence  
137 (PLP-LIF) technique within a temperature-controlled reactor (192 – 1100 K). A schematic  
138 diagram of the experimental layout is shown in Figure 2 of Mangan *et al.*<sup>27</sup> AIO molecules  
139 were produced in the reactor by the multiphoton dissociation of aluminium acetylacetonate  
140 ( $\text{Al}(\text{C}_5\text{H}_7\text{O}_2)_3$ , also known as  $\text{Al}(\text{acac})_3$ ) vapor by a loosely focused KrF excimer laser (Physik  
141 COMPEX 102) at 248 nm, with a typical pulse energy of 40 mJ at 10 Hz ( $< 5$  mJ in the reactor).  
142 Solid  $\text{Al}(\text{acac})_3$  powder was inserted into one of the chamber arms, contained in a steel boat  
143 attached to the end of a thermocouple (K-type), and heated to  $\sim 340$ - $370$  K using heating tape  
144 around the reactor arm in order to achieve a sufficient  $\text{Al}(\text{acac})_3$  vapour pressure, estimated to  
145 be  $2.4 \times 10^{-4}$  Torr at 340 K.<sup>28</sup> A flow of  $\text{N}_2$  over the steel boat entrained and transported the  
146  $\text{Al}(\text{acac})_3$  vapour into the main reactor volume. Experiments were conducted up to a maximum  
147 temperature around 780 K; above this temperature the LIF signal degraded, presumably due to  
148 decomposition of the  $\text{Al}(\text{acac})_3$  precursor in the reactor.

149 The transition probed by LIF was the AIO ( $\text{B}^2\Sigma^+ - \text{X}^2\Sigma^+(0,0)$ ) band at 484.23 nm<sup>29</sup> using a  
150 Nd:YAG (Quantel Q smart 850 at 355 nm) pumped dye laser (Sirah Cobra-stretch CBST-G-  
151 18) with Coumarin 102 laser dye. The time delay between the counter-propagating dye laser  
152 (probe) and excimer laser (photolysis,  $t = 0$ ) beams was varied to produce scans of the relative  
153 AIO concentration with time. Typical kinetic traces were produced from 1000 laser shots, with  
154 an accumulation time of 100 s. The AIO LIF signal was collected using a photomultiplier tube  
155 (Electron Tubes, model 9816QB) positioned orthogonal to the laser beams, through an  
156 interference filter ( $\lambda_{\text{max}} = 480$  nm, fwhm = 10 nm).

157 A total gas flow through the reactor of 180 - 600 sccm included the  $\text{Al}(\text{acac})_3$  vapor entrained  
158 in the bath gas, the reactant gas ( $\text{H}_2\text{O}$  or  $\text{H}_2$ ) and a balancing flow of the bath gas (either  $\text{N}_2$  or  
159 He). These flows were set using calibrated mass flow controllers, and the pressure in the reactor  
160 (4 – 24 Torr) measured with a capacitance manometer. The AIO concentration in the reactor  
161 was estimated to be  $\leq 10^{11}$  molecule  $\text{cm}^{-3}$ , based on the vapour pressure of  $\text{Al}(\text{acac})_3$  in the  
162 reactor side-arm (see above) being diluted by the other flows entering the reactor, and assuming  
163 at most 1% photolysis producing AIO. This AIO concentration was several orders of magnitude  
164 lower than the concentrations of  $\text{H}_2\text{O}$  or  $\text{H}_2$  in the reactor (e.g.  $[\text{H}_2\text{O}] = (0.02 - 1) \times 10^{15}$   
165 molecule  $\text{cm}^{-3}$ ) to ensure pseudo first-order conditions, consistent with the observed single  
166 exponential decays of AIO (see Results).

167 In the case of experiments studying R1, after each change of the  $\text{H}_2\text{O}$  gas flow the reactor was  
168 conditioned for 30 minutes. Repeat measurements of the first-order rate of AIO removal, taken  
169 several minutes apart, were used to confirm that the concentration of  $\text{H}_2\text{O}$  vapor in the reactor  
170 had reached a steady state, at which point the concentration was assumed to be consistent with  
171 that of the  $\text{H}_2\text{O}/\text{N}_2$  mixture made up on the glass gas-handling line.

172

173 **Materials.**  $\text{N}_2$  (99.9999% pure, Air Products) and He (99.9999 % pure, BOC) were used  
174 without any further purification.  $\text{H}_2$  (99.99 % pure, BOC) was flowed through a liquid  $\text{N}_2$  cold  
175 trap.  $\text{H}_2\text{O}$  vapor was produced by freeze-pump thawing deionized water for three cycles and  
176 subsequent dilution with  $\text{N}_2$  in a glass bulb.  $\text{Al}(\text{acac})_3$  (99% pure, Sigma Aldrich) was warmed  
177 under vacuum in the reactor for at least 30 mins prior to experiments.

178

179

180

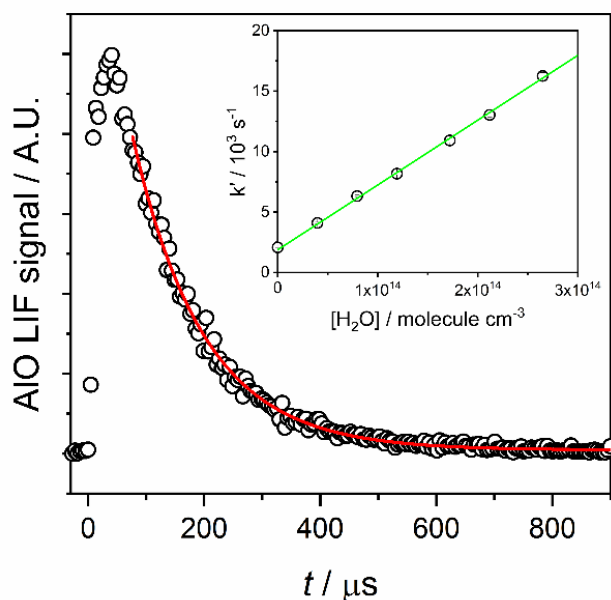
181 **Results**

182 **AlO + H<sub>2</sub>O**

183 The time-resolved LIF signals of AlO are described by a single exponential form  $A \cdot \exp(-k't)$ ,  
 184 where  $t$  is the time delay between the photolysis and probe lasers and  $k'$  is the pseudo first-  
 185 order decay coefficient. In the case of reaction R1, the rate equation is given by:

186 
$$k' = k_{\text{diff}} + k_{1a}[\text{H}_2\text{O}][\text{N}_2] + (k_{1b} + k_{1c} + k_d)[\text{H}_2\text{O}] \quad (\text{E1})$$

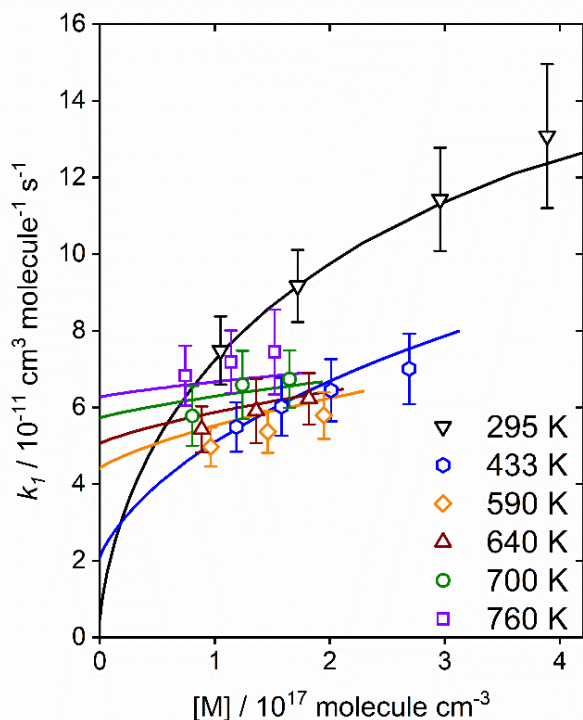
187 where  $k_{\text{diff}}$  is the rate of diffusion of AlO molecules out of the photolysis volume observed by  
 188 the PMT, as well as any reaction between AlO and the Al(acac)<sub>3</sub> precursor. As R1a is a  
 189 termolecular reaction the rate should be dependent on both the reactant [H<sub>2</sub>O] and bath gas  
 190 [N<sub>2</sub>]. Shown in the example kinetic trace of Figure 1 (and consistent with previous reactions  
 191 studied in Mangan *et al.*<sup>30</sup>), AlO is rapidly and directly made by photolysis of the precursor in  
 192 the absence of an O<sub>2</sub> flow, with the LIF signal peaking within ~ 40 μs. The more gradual rise  
 193 in the AlO LIF signal near the peak is likely caused by quenching of rovibrationally excited  
 194 AlO.<sup>25</sup> The kinetic traces were fitted at longer times ( $\geq 100 \mu\text{s}$ ) after which relaxation of the  
 195 excited states no longer significantly affects the single exponential nature of the decay,  
 196 ensuring pseudo first-order behaviour was observed.



197  
 198 **Figure 1.** Kinetic trace showing AIO LIF signal after PLP at  $t = 0 \mu\text{s}$  of Al(acac)<sub>3</sub> for [H<sub>2</sub>O] =  
 199  $1.19 \times 10^{14}$  molecules  $\text{cm}^{-3}$  at 590 K with a total pressure of 8.9 Torr. The inset shows the  
 200 associated bimolecular plot for R1 at all [H<sub>2</sub>O] measured at these conditions with  $k_1 =$   
 201  $(5.36 \pm 0.55) \times 10^{-11} \text{ cm}^3 \text{ molecule}^{-1} \text{ s}^{-1}$ .

202 Shown in the inset of Figure 1 is a plot of  $k'$  against [H<sub>2</sub>O], taken at 8.9 Torr at 590 K. The  
 203 slope of the linear fit provides the second order-rate coefficient  $k_1$ . The full set of measured  
 204 values are provided in Table S1 of the Supplementary Information. As was seen in Mangan *et*  
 205 *al.*<sup>30</sup>, the non-zero intercept  $k_{\text{diff}}$  is higher than the expected diffusion rate for AlO in N<sub>2</sub> under  
 206 these conditions,<sup>27</sup> because AlO is likely reacting with the precursor (or possibly a fragment of  
 207 Al(acac)<sub>3</sub> at higher temperatures). Repeat measurements of  $k'$  in the absence of reactant at the  
 208 beginning and end of each set of experiments were consistent within error. The second-order  
 209 rate coefficients were also independent of both gas residence time in the reactor (0.1 - 1 s) and  
 210 the precursor concentration, suggesting no interaction between the precursor and H<sub>2</sub>O.

211 Figure 2 shows the pressure dependence of  $k_1$  over the temperature range 295–760 K. At 295  
 212 K the reaction exhibits clear fall-off behaviour over the pressure range studied (3.2 - 12.1 Torr),  
 213 indicating that R1a is the dominant channel, and this also explains the negative  $T$ -dependence  
 214 up to 590 K. At higher temperatures the reaction exhibits little pressure dependence and  
 215 switches to a positive  $T$ -dependence, indicating that one or more of the bimolecular reaction  
 216 channels 1b – 1d has opened. This is explored further in the Discussion.



217  
 218 **Figure 2.** Pressure dependence of  $k_1$  (AlO + H<sub>2</sub>O) at 295 - 760 K in N<sub>2</sub> bath gas. The symbols  
 219 are experimental values, and the lines are Master Equation fits which include contributions  
 220 from R1a, R1b and R1c (see the Discussion).

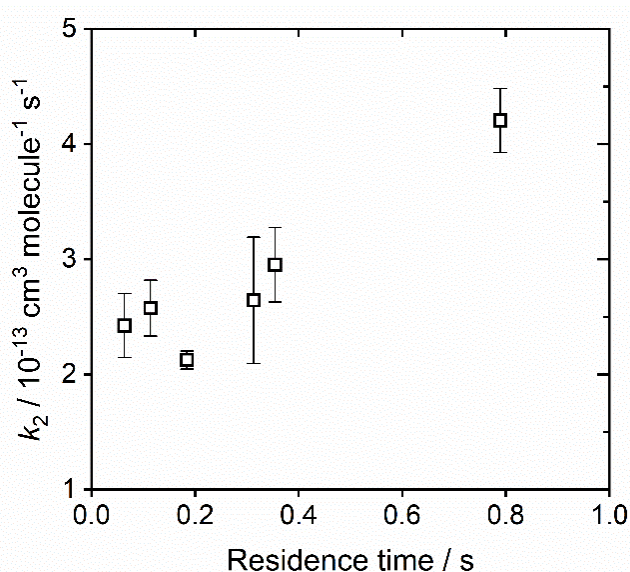
221  
 222 **AlO + H<sub>2</sub>**

223 The pseudo first-order decay of AlO in the presence of H<sub>2</sub> for the bimolecular reaction R2 can  
 224 be described by:

225 
$$k' = k_{diff} + k_2[\text{H}_2] \tag{E2}$$

226 Kinetic traces were satisfactorily fitted either using a single exponential decay after a time  
 227 delay (as described for R1 above), or using a bi-exponential to fit both the growth and loss of  
 228 the AlO signal, with both determinations of  $k'$  agreeing within error.  $k_2$  is much slower than  $k_1$   
 229 over the entire temperature range, so it was necessary to work with [H<sub>2</sub>] up to 3 orders of  
 230 magnitude larger than the [H<sub>2</sub>O] needed to study R1. At such high H<sub>2</sub> concentrations, it is  
 231 possible that secondary chemistry between H<sub>2</sub> and the precursor might result in reactive species  
 232 that remove AlO, and thus affect the determination of  $k_2$ . To investigate this possibility,  
 233 measurements of  $k_2$  were carried out over a range of residence times in the reactor for each  
 234 temperature. Changing the residence time was achieved by varying the ratios of total pressure  
 235 versus the total flow rate. An example plot of the measured value of  $k_2$  at 694 K versus the  
 236 residence time is shown in Figure 3, which illustrates that  $k_2$  increased by roughly a factor of 2

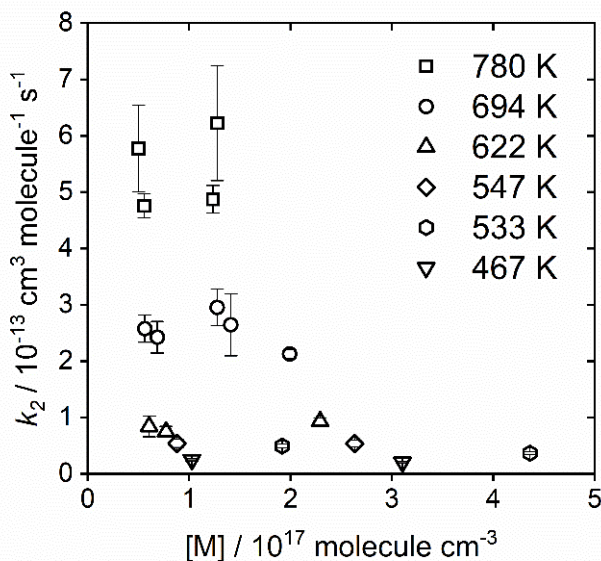
237 at the longest residence time (i.e. highest pressure:flow ratio). This suggests that secondary  
 238 chemistry between H<sub>2</sub> and the Al(acac)<sub>3</sub> precursor does produce a reactive species that removes  
 239 AIO, resulting in an overestimate of  $k_2$  at the longest residence times. Since the relationship  
 240 between the measured rate coefficient and the residence time is complex, extrapolating the  
 241 measured  $k_2$  to zero residence time is not straightforward. However, visual inspection of the  
 242 measured rates *vs* residence time at each temperature show that at the lowest residence times  
 243 the measured  $k_2$  becomes effectively independent of residence time, suggesting little or no  
 244 contribution from secondary chemistry. Thus, the final values reported for  $k_2$  at each  
 245 temperature are only those obtained at the shortest residence times, where the measured value  
 246 was essentially independent of residence time (Figure 3). The rates obtained using this visual  
 247 inspection method are in good agreement with rates obtained by extrapolating to zero residence  
 248 time using an exponential function, but are around 40% higher than rates obtained extrapolating  
 249 using a linear fit. The values of  $k_2$  over the range of temperature and pressure conditions studied  
 250 are listed in Table S1.



251  
 252 **Figure 3.** Bimolecular rate coefficients ( $k_2$ ) for R2 at 694 K measured at different reactor  
 253 residence times in s.

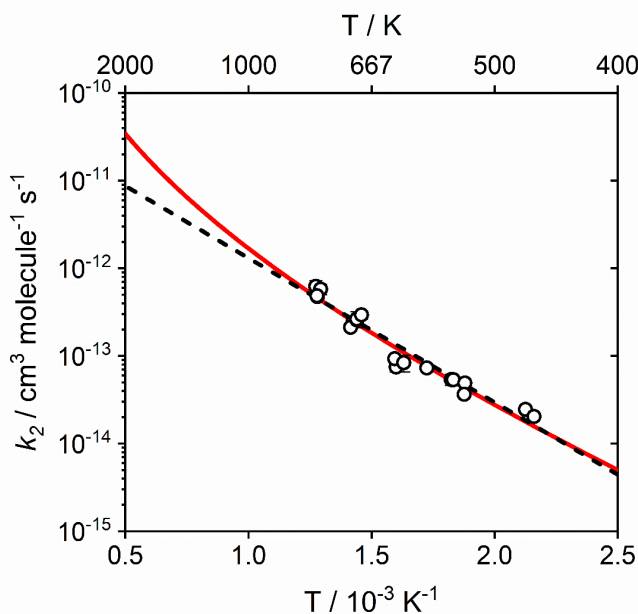
254 The other potential problem with having to use high concentrations of H<sub>2</sub> was the possible  
 255 presence of contaminants in the H<sub>2</sub>, specifically H<sub>2</sub>O and O<sub>2</sub> which recombine relatively rapidly  
 256 with AIO (see above and Mangan *et al.*<sup>30</sup>, respectively). To investigate this possibility and any  
 257 potential termolecular channel for H<sub>2</sub>, the pressure dependence of the AIO + H<sub>2</sub> reaction was  
 258 investigated. In Figure 4,  $k_2$  is plotted against total pressure (concentration [M]) over the  
 259 temperature range 467 - 780 K. A H<sub>2</sub>O leak on its own would only account for a 10 – 20%  
 260 change in  $k_2$  with pressure at each temperature studied, a change similar to the experimental  
 261 error. However, H<sub>2</sub>O contamination would have had to come from an air leak, so that the  
 262 recombination reaction of AIO with O<sub>2</sub> must also be included. If there had been a sufficient air  
 263 leak in the gas line from the H<sub>2</sub> cylinder to account for the measured  $k_2$ , this would have  
 264 produced an approximately 50% increase in  $k_2$  over the pressure range studied at 467 K, and  
 265 30% increase at 700 K. In fact, Figure 4 shows that no pressure dependent behaviour was  
 266 observed within the experimental uncertainty (only 10 - 20%). This indicates the absence of  
 267 both a significant leak and a termolecular channel for the H<sub>2</sub> reaction, further confirmed by  
 268 observing no difference in  $k_2$  measured with either N<sub>2</sub> or He as the bath gas (the former is  
 269 roughly twice as efficient as a third body<sup>31</sup>). At higher temperatures, the bimolecular channel

270 of AlO + H<sub>2</sub>O could play a role if the H<sub>2</sub> were contaminated with H<sub>2</sub>O from an air leak.  
 271 However, this point is discussed further - and ruled out - in the Discussion below.



272  
 273 **Figure 4.** Plot of  $k_2$  against the total concentration  $[M]$  in molecule  $\text{cm}^{-3}$  for the reaction of AlO  
 274 + H<sub>2</sub> at  $T = 467 - 780$  K.

275  
 276  $k_2$  was measured from 463 – 785 K, as shown in Figure 5. The low temperature limit was set  
 277 by the reaction becoming too slow at lower temperatures to measure with this system, and the  
 278 high temperature limit by decomposition of Al(acac)<sub>3</sub>. An Arrhenius fit to the dataset (dashed  
 279 line) yields  $k_2(463 - 785 \text{ K}) = (5.8 \pm 2.1) \times 10^{-11} \times \exp^{(-3792 \pm 215)/T} \text{ cm}^3 \text{ molecule}^{-1} \text{ s}^{-1}$ . The  
 280 theoretical fit to the dataset (red line) and subsequent extrapolation to the higher temperatures  
 281 pertinent for AGB stellar chemistry are discussed in the Discussion below.



282  
 283 **Figure 5.** Temperature dependence of the measured (open black circles) bimolecular rate  
 284 coefficients ( $k_2$ ) for AlO + H<sub>2</sub>. The dashed line is an Arrhenius fit to the experimental points  
 285 and the red solid line is a theoretical fit using RRKM theory (see the Discussion).

## 286 Discussion

287

288 The reaction between AlO and H<sub>2</sub>O (R1) does not appear to have been studied previously.  
289 However, in the case of AlO + H<sub>2</sub> (R2), Parnis *et al.*<sup>25</sup> measured an upper limit at 298 K of  $5$   
290  $\times 10^{-14}$  cm<sup>3</sup> molecule<sup>-1</sup> s<sup>-1</sup>, which is consistent with the extrapolated value of  $2 \times 10^{-16}$  cm<sup>3</sup>  
291 molecule<sup>-1</sup> s<sup>-1</sup> in the present study (using the Arrhenius expression determined in the Results  
292 section). The reaction between Al and H<sub>2</sub>O (R3) has been studied from 298 - 1174 K<sup>26</sup>. A  
293 number of theoretical studies of the potential energy surfaces connecting Al + H<sub>2</sub>O with AlO  
294 + H<sub>2</sub>, including transition state theory (TST) estimates of  $k_3$  and  $k_4$ , have been published over  
295 the past 50 years.<sup>32-34</sup> These studies have mainly been driven by interest in Al combustion  
296 chemistry.

297 In order to extrapolate the rate coefficients measured in the present study to temperatures above  
298 1000 K pertinent to stellar outflow chemistry, and also to determine product branching ratios,  
299 we combined electronic structure calculations of stationary points on the relevant PES with  
300 RRKM theory. Because reaction R3 (Al + H<sub>2</sub>O) occurs on parts of the same PES as R2 (AlO  
301 + H<sub>2</sub>), we also extrapolated the previous measurements of  $k_3$ <sup>26</sup> to higher temperatures. The  
302 geometries of the Al-containing molecules were first optimized at the B3LYP/6-311+g(2d,p)  
303 level of theory within the Gaussian 16 suite of programs,<sup>19</sup> and then accurate energies were  
304 determined at the G4 level of theory<sup>20</sup>. This level of theory was chosen because it is reasonably  
305 computationally efficient and in general appears to perform well on reactions involving small  
306 Al-containing molecules (though see below). For example, the reaction enthalpy for Al + O<sub>2</sub>  
307  $\rightarrow$  AlO + O is calculated at the G4 level to be  $\Delta H^\circ(0 \text{ K}) = -9.9$  kJ mol<sup>-1</sup>, in excellent agreement  
308 with the very high level (but computationally expensive) W1BD compound method,<sup>35</sup> which  
309 gives  $\Delta H^\circ(0 \text{ K}) = -10.2$  kJ mol<sup>-1</sup>. These values are consistent with the experimental value of  $-$   
310  $14 \pm 9$  kJ mol<sup>-1</sup>.<sup>23</sup>

311 The Cartesian coordinates, rotational constants, vibrational frequencies and heats of formation  
312 of the stationary points on the PESs for R1 and R2/R3 are listed in Tables S2 and S3,  
313 respectively. The PESs are shown in Figure 6, which also illustrates the geometries of these  
314 stationary points. The energies shown include zero-point energies, and this is why the energy  
315 of the saddle point labelled TS2 in Figure 6a appears slightly below that of the AlO-H<sub>2</sub>O  
316 adduct.

317 RRKM calculations were then performed using the Master Equation Solver for Multi-Energy  
318 well Reactions (MESMER) program.<sup>36</sup> Each reaction is assumed to proceed via the formation  
319 of an excited adduct, which can either dissociate or be stabilized by collision with the N<sub>2</sub> third  
320 body. The internal energy of this adduct was divided into a contiguous set of grains (typical  
321 width between 100 and 150 cm<sup>-1</sup>) containing a bundle of rovibrational states. Each grain was  
322 then assigned a set of microcanonical rate coefficients for dissociation, which were determined  
323 using inverse Laplace transformation to link them directly to  $k_{\text{rec},\infty}$ , the high pressure limiting  
324 recombination coefficient. The density of states of each adduct was calculated with the  
325 vibrational frequencies and rotational constants listed in Table S2 or S3, without making a  
326 correction for anharmonicity, and a classical densities of states treatment for the rotational  
327 modes. The microcanonical rate coefficients for reactions over barriers were treated using  
328 RRKM theory, with Eckart tunnelling applied where an H atom transfer occurred.<sup>36</sup>

329 The probability of collisional transfer between grains was estimated using the exponential  
330 down model, where the average energy for downward transitions is designated  $\langle \Delta E \rangle_{\text{down}}$ , and  
331 the probabilities for upward transitions are determined by detailed balance.<sup>31</sup>  $\langle \Delta E \rangle_{\text{down}}$  was  
332 assigned a small temperature dependence of the form  $T^\beta$ . The collision rate of N<sub>2</sub> with the

333 adduct as a function of temperature,  $Z(T)$ , was calculated using Lennard-Jones parameters ( $\sigma$   
 334 and  $\varepsilon$ ) to characterise the intermolecular potential. The Master Equation (ME), which describes  
 335 the evolution with time of the adduct grain populations, was then expressed in matrix form and  
 336 solved to yield the recombination rate constant at a specified pressure and temperature. The  
 337 adjustable parameters used to perform a global fit to all the experimental data points for each  
 338 reaction were  $k_{\text{rec},\infty}$ ,  $\sigma$ ,  $\langle\Delta E\rangle_{\text{down}}$  and  $\beta$ . Table 1 summarises the results.

339

340 **Table 1.** Parameters used in RRKM fits to the kinetics of reactions R1, R2 and R3.

Reaction	$\langle\Delta E\rangle_{\text{down}}$ cm <sup>-1</sup> at 298 K	$\beta^a$	$k_{\text{rec},\infty}$ cm <sup>3</sup> molecule <sup>-1</sup> s <sup>-1</sup>	$Z(T)^b$ cm <sup>3</sup> molecule <sup>-1</sup> s <sup>-1</sup>
AlO + H <sub>2</sub> O (R1)	290	-0.5	$7.0 \times 10^{-10} \exp(-265/T)$	$3.43 \times 10^{-10} (T/298)^{0.178}$
AlO + H <sub>2</sub> (R2)	300	0.0	Not applicable since first step is over a significant barrier – see Fig. 6(b)	$2.52 \times 10^{-10} (T/298)^{0.178}$
Al + H <sub>2</sub> O (R3)	300	0	$3.0 \times 10^{-11} (T/298)^{0.167}$	$2.52 \times 10^{-10} (T/298)^{0.178}$

341 <sup>a</sup>  $\langle\Delta E\rangle_{\text{down}}(T) = \langle\Delta E\rangle_{\text{down}}(T / 298)^\beta$

342 <sup>b</sup> Collision frequency between the adduct and N<sub>2</sub>. For R1,  $\sigma = 3.5 \text{ \AA}$  and  $\varepsilon/k_B = 300 \text{ K}$ ; for R2  
 343 and R3,  $\sigma = 3.0 \text{ \AA}$  and  $\varepsilon/k_B = 300 \text{ K}$ .

344

### 345 **AlO + H<sub>2</sub>O**

346 The recombination reaction R1a has a small submerged barrier (TS2 in Figure 6a) where the  
 347 initial AlO-H<sub>2</sub>O adduct rearranges to form the product Al(OH)<sub>2</sub>. The well is deep (-307 kJ mol<sup>-1</sup>  
 348 with respect to the reactants). Hence, the recombination is very fast, and is in the fall-off  
 349 region over the experimental pressure range (Figure 2). The fitted value of  $\langle\Delta E\rangle_{\text{down}}$  of 290  
 350 cm<sup>-1</sup> at 298 K is within the expected range for N<sub>2</sub>, along with the small temperature dependence  
 351 of  $\beta = -0.5$ .<sup>31</sup> The fitted Lennard-Jones parameters (footnote to Table 1) give  $Z(T)$  essentially  
 352 at the collision frequency. The fitted value of  $k_{\text{rec},\infty}$  for reaction R1 is a factor of ~2.4 times  
 353 smaller than the dipole-dipole capture rate between AlO and H<sub>2</sub>O, with a small positive  
 354 temperature dependence.

355 The rate coefficient  $k_{1a}$  can then be expressed by a Lindemann expression modified by a  
 356 broadening factor  $Fc$ <sup>37</sup>:  $\log_{10}(k_{1\text{rec},0} / \text{cm}^6 \text{ molecule}^{-2} \text{ s}^{-1}) = -32.9185 + 8.80276 \log_{10}(T) -$   
 357  $2.4723(\log_{10}(T))^2$ ;  $\log_{10}(k_{1\text{rec},\infty} / \text{cm}^3 \text{ molecule}^{-1} \text{ s}^{-1}) = -19.4686 + 7.62037 \log_{10}(T) -$   
 358  $1.47214(\log_{10}(T))^2$ ;  $Fc = 0.28$ , with an uncertainty of  $\pm 13\%$  within the experimental  
 359 temperature range (295 – 760 K).

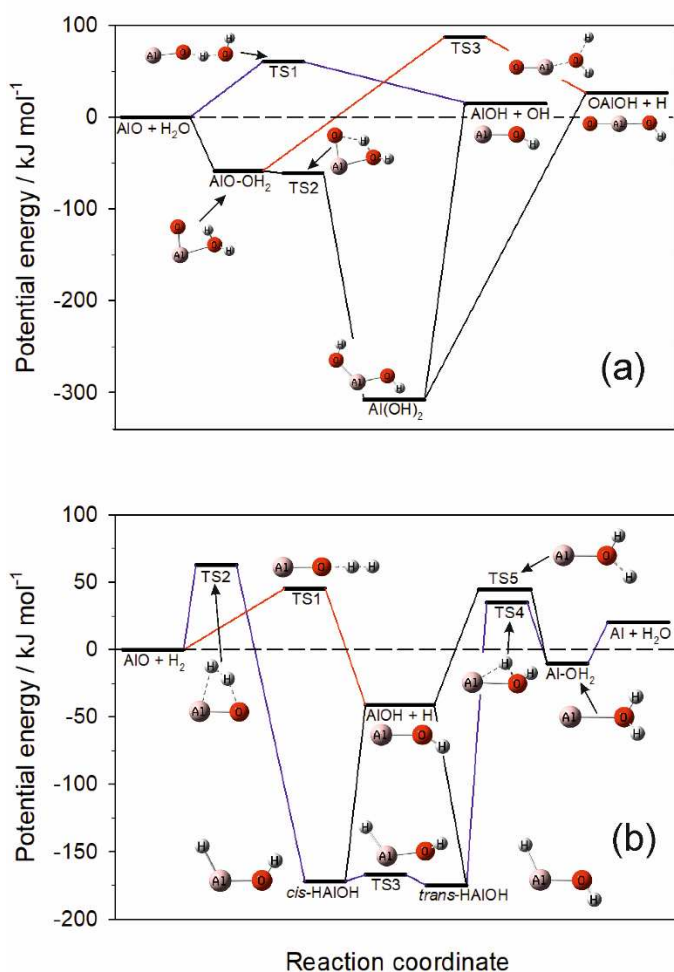
360 In terms of AlO chemistry in planetary atmospheres, the termolecular channel R1a will usually  
 361 not compete with recombination of AlO with significantly more abundant species such as O<sub>2</sub>  
 362 and CO<sub>2</sub> or, in the case of the terrestrial atmosphere, bimolecular reaction with O<sub>3</sub>.<sup>22, 30</sup>

363 The bimolecular reaction between AlO and H<sub>2</sub>O can form either AlOH (R1b), OAlOH (R1c)  
 364 or OAlO (R1d). Al(OH)<sub>2</sub> dissociates to AlOH without a barrier, although the overall reaction  
 365 enthalpy of R1b is 15 kJ mol<sup>-1</sup> endothermic. In contrast, the direct pathway via TS1 (blue route

366 in Figure 6a) involves a barrier of 60 kJ mol<sup>-1</sup> and so is uncompetitive. Channel R1c involves  
 367 either a direct reaction over a significant barrier (red route, TS3 at 87 kJ mol<sup>-1</sup>), or dissociation  
 368 of Al(OH)<sub>2</sub> to OAlOH + H which is endothermic by 26 kJ mol<sup>-1</sup> (Figure 6a). Reaction channel  
 369 1d to form OAlO + H<sub>2</sub> is very endothermic (111 kJ mol<sup>-1</sup>). Hence, reaction 1b to form AlOH  
 370 + OH via Al(OH)<sub>2</sub> is the dominant bimolecular reaction channel (>99% over the temperature  
 371 range 300 – 1600 K):

372  $k_{1b}(\text{AlO} + \text{H}_2\text{O} \rightarrow \text{AlOH} + \text{OH}) = (3.89 \pm 0.47) \times 10^{-10} \exp(-(1295 \pm 150)/T) \text{ cm}^3 \text{ molecule}^{-1}$   
 373 s<sup>-1</sup>.

374 This reaction channel will also very likely be too slow to be important in a planetary  
 375 atmosphere.



376  
 377 **Figure 6.** Potential energy surfaces for a) AlO + H<sub>2</sub>O and b) AlO + H<sub>2</sub>. The relative energies  
 378 include zero-point energy corrections. These are calculated using the G4 quantum chemistry  
 379 compound method.<sup>38</sup>

380

381

382 **AlO + H<sub>2</sub>**

383 The PES for this reaction is illustrated in Figure 6b. It is generally in good agreement with three  
 384 relatively recent theoretical studies,<sup>33, 34</sup> particularly with Sharipov *et al.*<sup>33</sup> who used G3

385 theory. The products AlOH + H can be formed directly through H atom abstraction via TS1,  
 386 or indirectly via insertion of the AlO into the H-H bond via TS2 to form *cis*-HAlOH or *trans*-  
 387 HAlOH (connected by TS3), which can then dissociate to AlOH + H. As shown in Figure 6b,  
 388 TS1 is 17 kJ mol<sup>-1</sup> lower than TS2, and so the direct pathway (red line in Fig. 6b) should be the  
 389 dominant pathway. In fact, it was not possible to match the experimental points with a TS1  
 390 barrier height of 45 kJ mol<sup>-1</sup> above the reactant energy. When this was reduced to 31 kJ mol<sup>-1</sup>,  
 391 a satisfactory fit was achieved to the experimental data points from the present study (Figure  
 392 5, red line). Although this difference of 14 kJ mol<sup>-1</sup> is greater than the average absolute  
 393 deviation of 5 kJ mol<sup>-1</sup> for energies of non-hydrogen molecules at the G4 level of theory,<sup>20</sup>  
 394 several of the significant outliers (> 10 kJ mol<sup>-1</sup> absolute difference) in that study are Al-  
 395 containing molecules.

396 A possible explanation for the measured rate of R2 being faster than predicted with the  
 397 calculated TS1 barrier of 45 kJ mol<sup>-1</sup> would be contamination of the H<sub>2</sub> with a leak of humid  
 398 lab air, since the bimolecular channel AlO + H<sub>2</sub>O (R1b) starts to become rapid above 500 K.  
 399 However, this possibility can be ruled out because the activation energy measured for *k*<sub>2</sub> is 32  
 400 kJ mol<sup>-1</sup>, which is much larger than the 11 kJ mol<sup>-1</sup> measured for *k*<sub>1b</sub> (see above). Moreover, to  
 401 account for the apparent rate increase at 540 K would require a 7.5% air contamination in the  
 402 H<sub>2</sub> flow (at the measured lab relative humidity of 40%). At the highest experimental  
 403 temperature of 785 K, the H<sub>2</sub> flow would need to be more than 50% contaminated with room  
 404 air to explain the difference between *k*<sub>2</sub> calculated using the G4 theory barrier height and the  
 405 measured value.

406 The best fit to the experimental points in Figure 5 gives (400 - 2000 K):

$$407 \quad k_2(\text{AlO} + \text{H}_2 \rightarrow \text{AlOH} + \text{H}) = (5.37 \pm 0.52) \times 10^{-13} (T/300)^{(2.77 \pm 0.19)} \exp(-2190 \pm 110/T)$$

$$408 \quad \text{cm}^3 \text{ molecule}^{-1} \text{ s}^{-1},$$

409 with an uncertainty of ±23% within the experimental temperature range (463 – 785 K). At 800  
 410 K, more than 99% of the reaction product is AlOH + H; 96.3% of the AlOH is formed via TS1,  
 411 2.3% from dissociation of *cis*-HAlOH, and 1.4% from dissociation of *trans*-HAlOH. The other  
 412 product, Al + H<sub>2</sub>O which is produced via the blue route in Figure 6b, is negligible (0.008%)

413

#### 414 **Al + H<sub>2</sub>O and AlOH + H**

415 The same PES for reaction R2 can now be used to estimate rate coefficients for *k*<sub>3</sub> and *k*<sub>4</sub>. As  
 416 shown in Figure 7a, a satisfactory fit to the experimental measurements of McClean *et al.*<sup>26</sup> is  
 417 achieved, yielding (250-1200 K):

$$418 \quad k_3(\text{Al} + \text{H}_2\text{O} \rightarrow \text{AlOH} + \text{OH}) = (1.7 \pm 0.2) \times 10^{-12} \exp(-422 \pm 50/T) + (1.5 \pm 0.4) \times 10^{-10} \exp(-$$

$$419 \quad (2657 \pm 190)/T) \text{ cm}^3 \text{ molecule}^{-1} \text{ s}^{-1}.$$

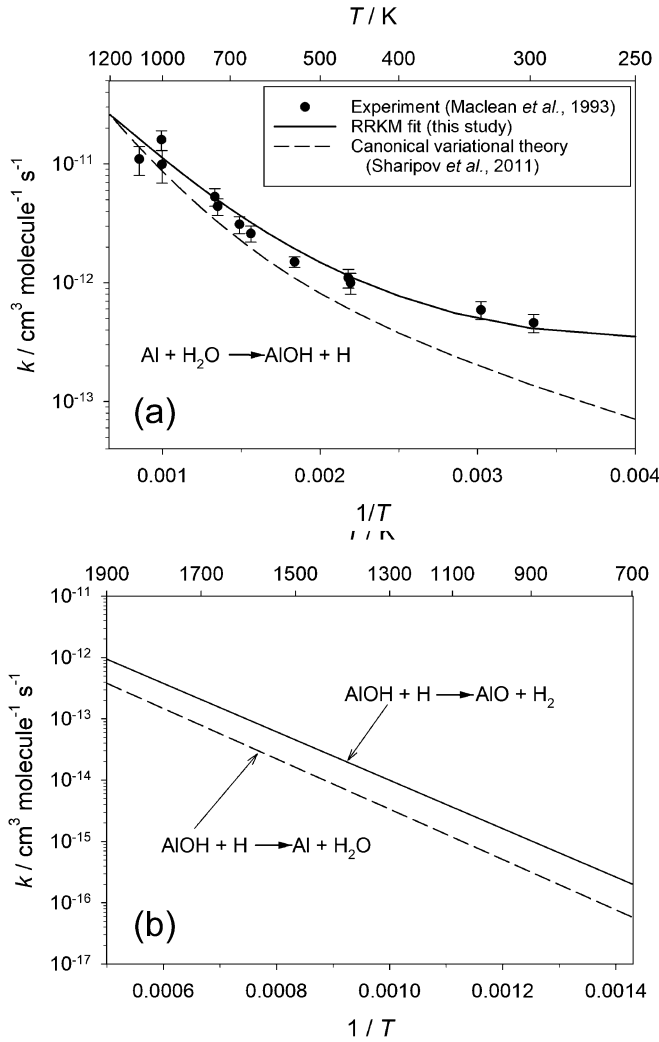
420 The MESMER calculation captures the experimental data below 600 K significantly better than  
 421 the canonical variational theory fit of Sharipov *et al.*<sup>33</sup>, as shown in Figure 7a. AlOH is  
 422 predicted to be the only significant product (>99%). At 300 K, 19% of the AlOH is formed via  
 423 TS5 (Figure 6b), 42% via TS4 and *trans*-HAlOH, and 39% via TS3, TS4 and *cis*-AlOH. The  
 424 amount of AlO, formed via TS4, TS3 and TS2, is negligible ( $1.8 \times 10^{-4}$  %).

425 The calculated rate coefficients for the two reaction channels of AlOH + H (R4) are shown as  
 426 a function of temperature in Figure 7b. Arrhenius behaviour is predicted from 700 – 2000 K:

$$427 \quad k_{4a}(\text{AlOH} + \text{H} \rightarrow \text{AlO} + \text{H}_2) = 8.89 \times 10^{-11} \exp(-9092/T) \text{ cm}^3 \text{ molecule}^{-1} \text{ s}^{-1}$$

$$428 \quad k_{4b}(\text{AlOH} + \text{H} \rightarrow \text{Al} + \text{H}_2\text{O}) = 4.31 \times 10^{-11} \exp(-9457/T) \text{ cm}^3 \text{ molecule}^{-1} \text{ s}^{-1}$$

429 The ratio of AlO to Al product ranges from 2.5 to 3.5 over this temperature range. For channel  
 430 R4a at 1300 K, AlO + H<sub>2</sub> is produced via TS1 (94%) and TS2 (6%); for channel R4b, Al +  
 431 H<sub>2</sub>O is produced via TS4 (52%) and TS5 (48%) (see Figure 6b). For reasons that are unclear,  
 432 although the activation energy of 8762 K calculated by Sharipov *et al.*<sup>33</sup> for  $k_{4a}$  is in good  
 433 agreement with the present result, the pre-exponential factor (between 700 and 2000 K) is a  
 434 factor of 260 times smaller. That study did not consider the other significant channel which  
 435 produces Al + H<sub>2</sub>O (R4b).



436 **Figure 7.** (a) RRKM fit (black line) to the experimental rate coefficients (points with error  
 437 bars) from Maclean *et al.*<sup>26</sup> for the reaction between Al and H<sub>2</sub>O. A canonical variational  
 438 theory fit from Sharipov *et al.*<sup>33</sup> is also shown. (b) Theoretical rate coefficients for the reaction  
 439 of AIOH with H, producing either Al + H<sub>2</sub>O or AlO + H<sub>2</sub>.

441

#### 442 Implications on the chemistry of AlO and AIOH around an AGB star

443 We now incorporate these results on R1 – R4 in a model of the outflow from an AGB star,  
 444 where the radial position  $r$  from the star is expressed as a factor of  $R_*$  (where  $1R_*$  is the radius  
 445 at the stellar surface). As an example, we consider a Semi-Regular Variable (SRV) star.<sup>39</sup> Here  
 446 we model the stellar outflow with a beta-velocity law, which takes into account the net  
 447 acceleration of the wind without explicitly considering pulsations:

$$448 \quad v_\beta(r) = v_0 + (v_\infty - v_0)(1 - R_*/r)^\beta \quad (\text{E3})$$

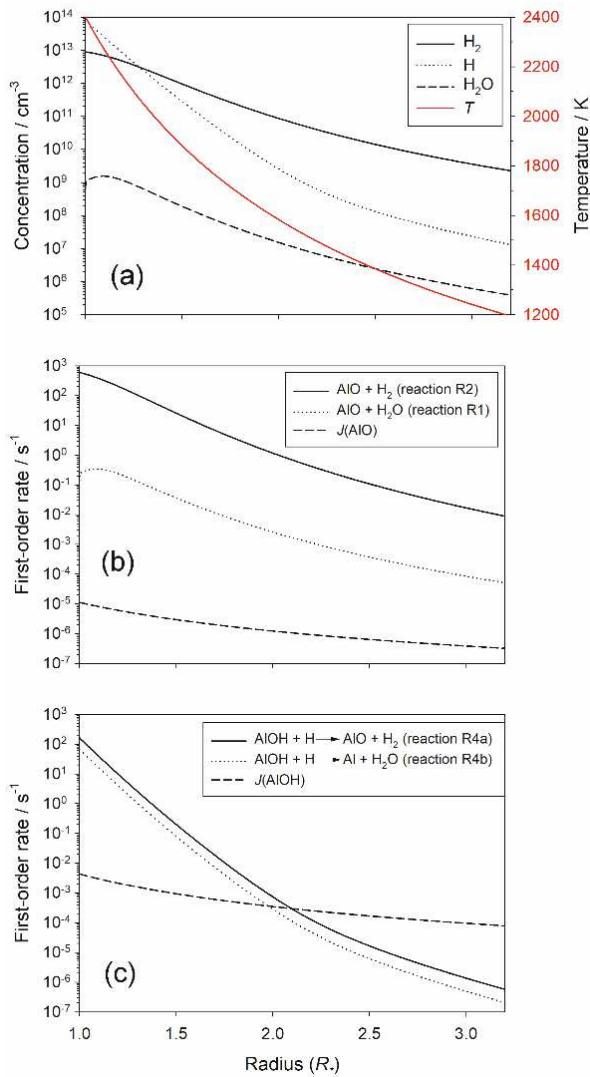
449 where  $v_\infty$  is the terminal velocity, which is  $5.7 \text{ km s}^{-1}$  for the SRV model,<sup>14</sup>  $v_0 = v(R_*) = 1.5 \text{ km}$   
 450  $\text{s}^{-1}$  is the initial velocity at the stellar surface  $R_* (= 2.5 \times 10^{13} \text{ cm})$ , and the parameter  $\beta = 1$ . The  
 451 temperature profile is given as a power-law with an exponent  $\alpha = 0.6$  and the density is  
 452 expressed using the pressure scale height  $H = RT R_*^2 / (\mu M_* G)$ , the Ideal Gas Law, and a  
 453 parameter  $\gamma = 0.89$  (for details, see e.g. Gobrecht *et al.*<sup>16</sup> and references therein):

454 
$$T(r) = T_*(r/R_*)^{-\alpha} \tag{E4}$$

455 and 
$$n(r) = n_* \exp((R_*(1 - \gamma^2)/(H(1 - \alpha)) (1 - r/R_*)^{\alpha-1}) \tag{E5}$$

456 The surface pressure  $n_* = 10^{14} \text{ cm}^{-3}$  and the effective temperature  $T_*$  is 2400 K.

457 The chemistry is modelled using a kinetic network which is solved with the FORTRAN routine  
 458 LSODE.<sup>40</sup> The network includes 40 neutral molecular species and 105 reactions pertaining to  
 459 the circumstellar environments of O-rich stars. Here, we assume a C/O ratio of 0.75  
 460 corresponding to the FRUITY stellar evolution model of a solar metallicity ( $Z=0.014$ ) star with  
 461 an initial mass of  $1.5 M_*$ , having experienced 3 (out of a total of 5) dredge-up mixing  
 462 episodes.<sup>41</sup> The species in the network include the prevalent species  $\text{H}_2$ ,  $\text{H}$ ,  $\text{CO}$ ,  $\text{CO}_2$ ,  $\text{H}_2\text{O}$ ,  $\text{OH}$   
 463 and  $\text{SiO}$ .<sup>42</sup> The rate coefficients are adopted from the NIST kinetics database.<sup>43</sup> The densities  
 464 of  $\text{H}_2$ ,  $\text{H}$  and  $\text{H}_2\text{O}$  (relevant for R1 to R4), as well as the temperature  $T$ , are illustrated in Figure  
 465 8a as a function of radial position expressed as a factor of  $R_*$ .

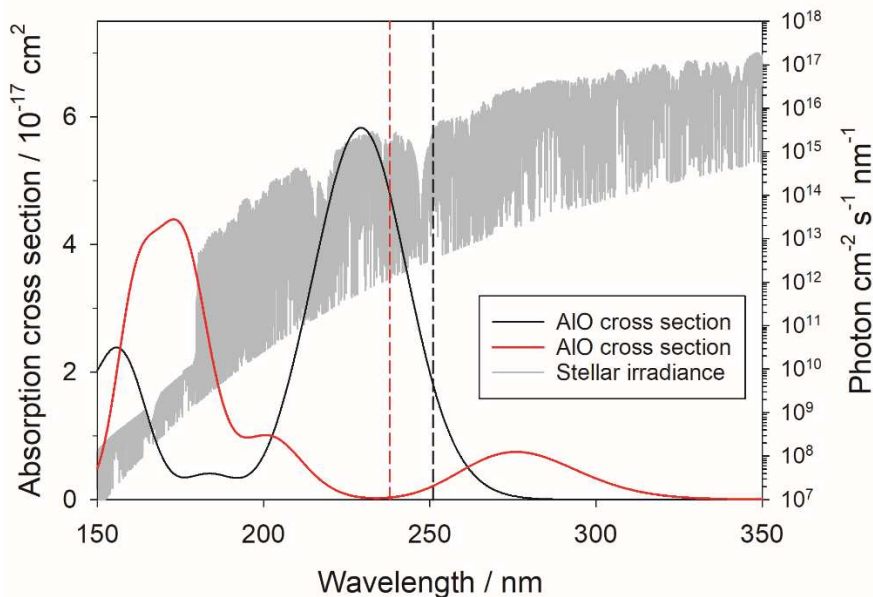


466

467 **Figure 8.** (a) Predicted densities of H<sub>2</sub>, H, H<sub>2</sub>O and  $T$  as a function of radial position for the  $\beta$ -  
 468 velocity trajectory model of a SRV star. (b) and (c) First-order removal rates of AIO and AIOH,  
 469 respectively, as a function of radius.

470 The photolysis rates of AIOH and AIO were computed by using the time-dependent density  
 471 function theory (TD-DFT) method<sup>44</sup> to calculate the vertical excitation energies and transition  
 472 dipole moments for transitions from the ground state of each molecule up to the first 30  
 473 electronically excited states. The resulting absorption cross sections are illustrated in Figure 9.  
 474 Each cross section was then convolved up to its dissociation threshold with a model stellar  
 475 irradiance flux from the MARCS data-base for an evolved star with  $T^* = 2500$  K (the lowest  
 476 stellar  $T^*$  in the MARCS data-base).<sup>45</sup> The irradiance spectrum is plotted in Figure 9. The  
 477 photolysis threshold was set to correspond to the bond dissociation energy at the G4 level of  
 478 theory, which is an upper wavelength limit. This is because a photon with more than the bond  
 479 energy may be required depending on the position of the upper dissociating electronic states,  
 480 which have been explored in detail by Trabelsi and Francisco<sup>46</sup>. These thermodynamic  
 481 thresholds are illustrated in Figure 9. When computing the photolysis rate as a function of  
 482 increasing temperature, the threshold was red-shifted to take account of the increasing internal  
 483 energy of the molecule. We also assume here that AIOH photolyses to AIO + H rather than AI  
 484 + OH (which is 76 kJ mol<sup>-1</sup> higher in energy).

485 The resulting first-order photolysis rates are then:  $J(\text{AIOH}) = 1.5 \times 10^{-4} \exp(1.40 \times 10^{-3} T)$ ,  
 486 and  $J(\text{AIO}) = 9.7 \times 10^{-7} \exp(1.02 \times 10^{-3} T)$  at  $1R^*$ . At a temperature of 2000 K, photolysis of  
 487 AIOH is predicted to be 500 times faster than photolysis of AIO. This arises because although  
 488 AIO has relatively large absorption features in the near-UV/visible, these are beyond its  
 489 photolysis threshold, and stellar irradiance falls rapidly in the near UV (Figure 9). We assume  
 490 that in the inner wind the dust-to-gas ratio is too small<sup>5, 16</sup> for optical extinction by dust to  
 491 significantly attenuate these rates.



492 **Figure 9.** Absorption cross sections of AIOH and AIO computed using time-dependent density  
 493 function theory.<sup>19</sup> The vertical dashed lines indicate the photolysis thresholds at 252 and 237  
 494 nm, respectively, computed from the relevant bond dissociation energies. Also shown (right-  
 495 hand ordinate axis) is the spectral irradiance at the surface of an evolved star with an effective  
 496 temperature of 2500 K, derived from the MARCS data-base.<sup>45</sup>

498

499 Figure 8(b) and (c) show the first-order removal rates of AlO and AlOH, respectively, as a  
 500 function of  $r$ . The reaction rates generally decrease with stellar distance because of the  
 501 decreasing densities of the excess reactants ( $\text{H}_2$ , H and  $\text{H}_2\text{O}$ ) and temperature (Figure 8a).  
 502  $J(\text{AlO})$  and  $J(\text{AlOH})$  decrease as  $r^2$ . With the caveat that  $J(\text{AlOH})$  is an upper limit, this  
 503 photolysis rate could exceed the rate of reaction of AlOH with H (R4) at distances larger than  
 504  $\sim 2.2R_*$  (Figure 8c).

505 Note that the first-order rates in Figure 8 are faster than  $10^{-7} \text{ s}^{-1}$  at distances out to  $3R_*$ . The  
 506 expansion rate of the outflow is given by  $v_\beta(r)/r$ , which varies between  $7 \times 10^{-9}$  and  $5 \times 10^{-9} \text{ s}^{-1}$   
 507 over this distance. Hence, the rate of chemical conversion between AlO, AlOH and Al is much  
 508 faster than the expansion rate, and the kinetic steady state approximation can be applied. For  
 509 this simple model which only involves these three Al-containing species, the total Al density  
 510  $[\text{Al}]_{\text{total}} = [\text{Al}] + [\text{AlO}] + [\text{AlOH}]$ , which we set equal to its photospheric abundance  $2.82 \times 10^{-6}$   
 511 relative to H ( $= 2[\text{H}_2] + [\text{H}]$ ).<sup>47</sup> At steady-state,

512

$$513 \quad [\text{AlOH}] = [\text{Al}_{\text{total}}] / \left( 1 + \frac{k_{4b}[\text{H}]}{k_3[\text{H}_2\text{O}]} + \left( 1 + \frac{J_{\text{AlO}}}{k_3[\text{H}_2\text{O}]} \right) \left( \frac{k_{4a}[\text{H}] + J_{\text{AlOH}}}{k_{1b}[\text{H}_2\text{O}] + k_{2a}[\text{H}_2] + J_{\text{AlO}}} \right) \right) \quad (\text{E6})$$

514

$$515 \quad [\text{AlO}] = \left( \frac{k_{4a}[\text{H}] + J_{\text{AlOH}}}{k_{1b}[\text{H}_2\text{O}] + k_{2a}[\text{H}_2] + J_{\text{AlO}}} \right) [\text{AlOH}] \quad (\text{E7})$$

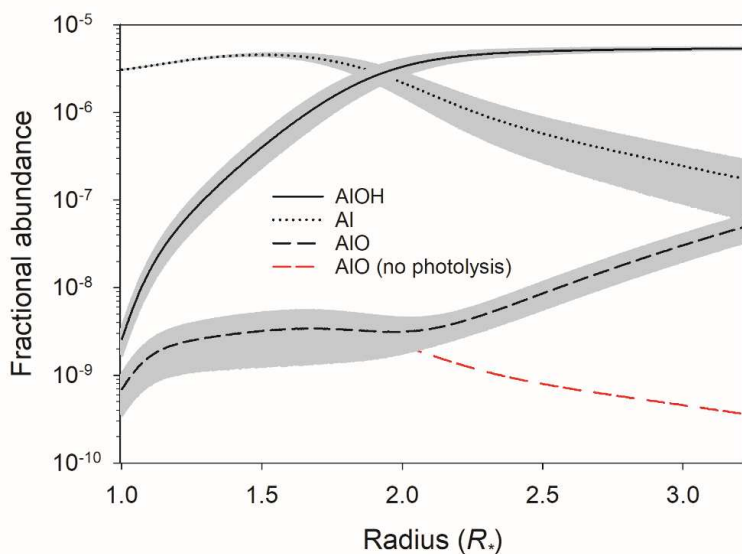
516

$$517 \quad \text{and} \quad [\text{Al}] = [\text{Al}_{\text{total}}] - [\text{AlOH}] - [\text{AlO}] \quad (\text{E8})$$

518

519 Figure 10 illustrates the abundances of Al, AlO and AlOH with respect to the total gas density  
 520 (i.e.  $[\text{H}] + [\text{H}_2]$ ), as a function of  $r$ . The uncertainty envelopes for each species were determined  
 521 using a Monte Carlo procedure to calculate the standard deviations of 1000 model runs in which  
 522  $k_{1b}$ ,  $k_{2a}$ , and  $k_3$  were randomly sampled within their  $1\sigma$  uncertainties (using the uncertainties in  
 523 the rate coefficient expressions in the earlier parts of the Discussion).  $k_{4a}$  and  $k_{4b}$  were estimated  
 524 by detailed balance with  $k_{2a}$  and  $k_3$ , respectively, including random sampling within a  $\pm 6 \text{ kJ}$   
 525  $\text{mol}^{-1}$  uncertainty in the reaction enthalpies of R2a and R3 (the expected uncertainty of G4  
 526 theory<sup>20</sup>). AlOH becomes the most abundant Al species at  $r > 1.8R_*$ , tracking the increasing  
 527 ratio of  $\text{H}_2$  to H which exceeds unity at around  $1.3R_*$  (Figure 9a), allowing R2 to dominate over  
 528 R4.

529 The red dashed line in Figure 10 shows the AlO profile when photolysis is turned off: this  
 530 relatively minor species decreases by about two orders of magnitude at a distance of  $3R_*$ . The  
 531 corresponding change in AlOH is relatively small (increase of only 0.8%) because it is already  
 532 overwhelmingly the dominant Al species. Recent observations<sup>14, 48</sup> have detected AlO in the  
 533 inner winds of SRV type stars with abundances of the order of  $10^{-8}$ . The modelled AlO  
 534 approaches  $3 \times 10^{-8}$  at  $3R_*$  (Figure 10), and so is clearly in accord with these observations. Even  
 535 without photolysis, AlO reaches  $3 \times 10^{-9}$  at  $1.6R_*$ , which is only a factor of 3 below the  
 536 observations (which in turn are quite uncertain because of assumptions that have to be made  
 537 about thermodynamic quantities in the CSE).



538

539 **Figure 10.** Fractional abundances of AlOH, AIO and Al with respect to the total gas density  
 540 (i.e.  $H + H_2$ ), as a function of the radial position  $R^*$  (black curves, filled grey areas are  
 541 uncertainty envelopes), predicted by the SRV model with a  $\beta$ -velocity trajectory and steady-  
 542 state kinetics. The red dashed line indicates the AIO abundance when photolysis of AlOH and  
 543 AIO is turned off.

544

545 In contrast, observations of AlOH around AGB stars show that the abundance of this molecule  
 546 is  $\leq 10^{-7}$ ,<sup>14</sup> compared with a value of  $5 \times 10^{-6}$  in our model. There are two likely reasons for  
 547 the model overprediction by a factor of more than 50: first is that pulsation-induced shocks,<sup>16</sup>  
 548 which involve rapid heating that would recycle the AlOH to Al, are not included in our simple  
 549 outflow model; and second, much of the Al eventually becomes locked up in alumina  
 550 nanoparticles (see the Introduction), rather than remaining in the gas phase.

551 Finally, Figure 10 shows that the  $[AIO]/[AlOH]$  ratio beyond  $1.8R^*$  depends strongly on the  
 552 inclusion of AlOH photolysis. An experimental measurement of the AlOH photolysis cross  
 553 section should therefore be a priority in future laboratory work.

554

## 555 Conclusions

556 The reactions of AIO with  $H_2O$  and  $H_2$  were measured using the PLP-LIF technique in a  
 557 temperature-controlled slow flow reactor. The full set of measured rate coefficients for the  
 558 reactions  $AIO + H_2O$  (R1) and  $AIO + H_2$  (R2) are listed in Table S1. These reactions were  
 559 shown to occur via multiple pathways over complex potential energy surfaces. The surface for  
 560 R2 also describe the reactions between  $Al + H_2O$  (R3) and  $AlOH + H$  (R4). Satisfactory fits of  
 561 a Master Equation solver for reactions with multiple energy wells to the experimental data  
 562 provide the rate coefficient expressions for R1 – R4 summarized in Table 2. These are  
 563 appropriate for modelling Al chemistry in stellar outflows and planetary upper atmospheres.

564 In the inner region of the outflow from an evolved star, where not enough dust has been  
 565 produced to cause significant optical extinction in the near-UV, the photolysis of AlOH and  
 566 AIO needs to be considered. Upper limits to the photolysis rates of these molecules were  
 567 estimated by calculating their absorption cross sections and setting the photodissociation  
 568 threshold equal to the relevant bond energy, as well as assuming that AlOH only photolyses to

569 AIO. The stellar outflow chemistry of Al was then investigated using a  $\beta$ -trajectory model of a  
 570 Semi-Regular Variable AGB star, where the kinetic steady-state approximation is valid. This  
 571 relatively simple model predicts that AlOH is the major gas-phase Al species beyond two  
 572 stellar radii, and shows that the relative AIO abundance is very sensitive to the AlOH photolysis  
 573 rate.

574

575 **Table 2.** Summary of rate coefficients determined in this study.

Reaction	Rate coefficient <sup>a</sup>
R1a AIO + H <sub>2</sub> O (+ N <sub>2</sub> ) → Al(OH) <sub>2</sub>	$\log_{10}(k_{\text{rec},0} / \text{cm}^6 \text{ molecule}^{-2} \text{ s}^{-1}) = -32.9185 + 8.80276 \log_{10}(T) - 2.4723(\log_{10}(T))^2$ ; $\log_{10}(k_{\text{rec},\infty} / \text{cm}^3 \text{ molecule}^{-1} \text{ s}^{-1}) = -19.4686 + 7.62037 \log_{10}(T) - 1.47214(\log_{10}(T))^2$ ; $F_c = 0.28$ (uncertainty $\pm 13\%$ from 295 – 760 K)
R1b AIO + H <sub>2</sub> O → AlOH + OH	$(3.89 \pm 0.47) \times 10^{-10} \exp(-(1295 \pm 150)/T)$
R2a AIO + H <sub>2</sub> → AlOH + H	$(5.37 \pm 0.52) \times 10^{-13} (T/300)^{(2.77 \pm 0.19)} \exp(-(2190 \pm 110)/T)$
R3 Al + H <sub>2</sub> O → AlOH + H	$(1.7 \pm 0.2) \times 10^{-12} \exp(-(422 \pm 50)/T) + (1.5 \pm 0.4) \times 10^{-10} \exp(-(2657 \pm 190)/T)$
R4a AlOH + H → AIO + H <sub>2</sub>	$8.89 \times 10^{-11} \exp(-9092/T)$ <sup>b</sup>
R4b AlOH + H → Al + H <sub>2</sub> O	$4.31 \times 10^{-11} \exp(-9457/T)$ <sup>b</sup>

576 <sup>a</sup> Units for bimolecular reactions:  $\text{cm}^3 \text{ molecule}^{-1} \text{ s}^{-1}$ . <sup>b</sup> Theoretical estimates, not fitted to  
 577 experimental data.

578

579

580 **Supporting Information:** Table S1 provides a list of second-order rate coefficients measured  
 581 for reactions R1 and R2, as a function of temperature and pressure (and bath gas for R2). Table  
 582 S2 lists the molecular properties and heats of formation (at 0 K) of the stationary points on the  
 583 AIO + H<sub>2</sub>O potential energy surface. Table S3 lists the molecular properties and heats of  
 584 formation (at 0 K) of the stationary points on the AIO + H<sub>2</sub> potential energy surface.

585

## 586 Acknowledgements

587 This work was supported by the European Research Council (Consolidator grant  
 588 646758AEROSOL) and the UK Natural Environment Research Council (Grant Number  
 589 NE/P001815/1). The kinetic data and the parameters used in the theoretical calculations are  
 590 provided in the Supporting Information. The data plotted in Figures 8 -10 is available at  
 591 doi:10.5281/zenodo.5017759.

592

593

594

595

596 **References**

- 597 (1). Gail, H. P.; Zhukovska, S. V.; Hoppe, P.; Trieloff, M. Stardust from asymptotic giant  
598 branch stars. *Astrophys. J.* **2009**, *698*, 1136-1154.
- 599 (2). Gehrz, R. D. Sources of Stardust in the Galaxy. In *Interstellar Dust. International*  
600 *Astronomical Union*, Allamandola, L. J.; Tielens, A. G. G. M., Eds. Springer, Dordrecht:  
601 1989; Vol. 135, pp 445-453.
- 602 (3). Bromley, S. T.; Martin, J. C. G.; Plane, J. M. C. Under what conditions does (SiO)<sub>N</sub>  
603 nucleation occur? A bottom-up kinetic modelling evaluation. *Phys. Chem. Chem. Phys.* **2016**,  
604 *18*, 26913-26922; Gail, H. P.; Wetzel, S.; Pucci, A.; Tamanai, A. Seed particle formation for  
605 silicate dust condensation by SiO nucleation. *Astron. Astrophys.* **2013**, *555*, art. no.: A119;  
606 Gail, H. P.; Sedlmayr, E. Mineral formation in stellar winds. I. Condensation sequence of  
607 silicate and iron grains in stationary oxygen rich outflows. *Astron. Astrophys.* **1999**, *347*, art.  
608 no.: 594; Plane, J. M. C. On the nucleation of dust in oxygen-rich stellar outflows. *Phil.*  
609 *Trans. Roy. Soc. A* **2013**, *371*, art. no.: 20120335.
- 610 (4). Sargent, B. A. Alumina Polymorphism in the Circumstellar Dust Shells of Asymptotic  
611 Giant Branch Stars. *Astrophys. J.* **2018**, *866*, art. no.: L1.
- 612 (5). Karovicova, I.; Wittkowski, M.; Ohnaka, K.; Boboltz, D. A.; Fossat, E.; Scholz, M. New  
613 insights into the dust formation of oxygen-rich AGB stars. *Astron. Astrophys.* **2013**, *560*, art.  
614 no.: A75.
- 615 (6). Onaka, T.; de Jong, T.; Willems, F. J. A study of M Mira variables based on IRAS LRS  
616 observations. I. Dust formation in the circumstellar shell. *Astron. Astrophys.* **1989**, *218*, 169-  
617 179.
- 618 (7). Takigawa, A.; Kamizuka, T.; Tachibana, S.; Yamamura, I. Dust formation and wind  
619 acceleration around the aluminum oxide-rich AGB star W Hydrae. *Science Adv.* **2017**, *3*, art.  
620 no.: eaao2149.
- 621 (8). Begemann, B.; Dorschner, J.; Henning, T.; Mutschke, H.; Gurtler, J.; Kompe, C.; Nass,  
622 R. Aluminum oxide and the opacity of oxygen-rich circumstellar dust in the 12-17 micron  
623 range. *Astrophys. J.* **1997**, *476*, 199-208.
- 624 (9). Posch, T.; Kerschbaum, F.; Mutschke, H.; Fabian, D.; Dorschner, J.; Hron, J. On the  
625 origin of the 13  $\mu$  m feature - A study of ISO-SWS spectra of oxygen-rich AGB stars.  
626 *Astron. Astrophys.* **1999**, *352*, 609-618.
- 627 (10). Sloan, G. C.; Kraemer, K. E.; Goebel, J. H.; Price, S. D. Guilt by association: The 13  
628 micron dust emission feature and its correlation to other gas and dust features. *Astrophys. J.*  
629 **2003**, *594*, 483-495.
- 630 (11). Jones, O. C.; Kemper, F.; Srinivasan, S.; McDonald, I.; Sloan, G. C.; Zijlstra, A. A.  
631 Modelling the alumina abundance of oxygen-rich evolved stars in the Large Magellanic  
632 Cloud. *Mon. Not. Roy. Astron. Soc.* **2014**, *440*, 631-651.
- 633 (12). Tenenbaum, E. D.; Ziurys, L. M. Exotic Metal Molecules in Oxygen-rich Envelopes:  
634 Detection of AlOH ( $X^1\Sigma^+$ ) in VY Canis Majoris. *Astrophys. J. Lett.* **2010**, *712*, art. no.: L93.

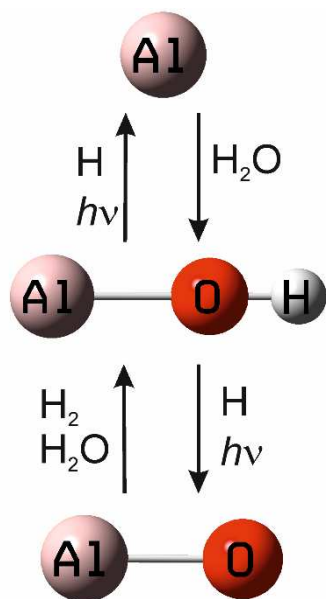
- 635 (13). Kamiński, T.; Wong, K. T.; Schmidt, M. R.; Müller, H. S. P.; Gottlieb, C. A.;  
636 Cherchneff, I.; Menten, K. M.; Keller, D.; Brünken, S.; Winters, J. M., et al. An observational  
637 study of dust nucleation in Mira (o Ceti) I. Variable features of AlO and other Al-bearing  
638 species. *Astron. Astrophys.* **2016**, 592, art. no.: A42; De Beck, E.; Decin, L.; Ramstedt, S.;  
639 Olofsson, H.; Menten, K. M.; Patel, N. A.; Vlemmings, W. H. T. Search for aluminium  
640 monoxide in the winds of oxygen-rich AGB stars. *Astron. Astrophys.* **2017**, 598, art. no.:  
641 A53.
- 642 (14). Decin, L.; Richards, A. M. S.; Waters, L. B. F. M.; Danilovich, T.; Gobrecht, D.;  
643 Khouri, T.; Homan, W.; Bakker, J. M.; Van de Sande, M.; Nuth, J. A., et al. Study of the  
644 aluminium content in AGB winds using ALMA. *Astron. Astrophys.* **2017**, 608, art. no.: A55.
- 645 (15). Tachibana, S.; Kamizuka, T.; Hirota, T.; Sakai, N.; Oya, Y.; Takigawa, A.; Yamamoto,  
646 S. Spatial Distribution of AlO in a High-mass Protostar Candidate Orion Source I. *Astrophys.*  
647 *J.* **2019**, 875, art. no.: L29.
- 648 (16). Gobrecht, D.; Cherchneff, I.; Sarangi, A.; Plane, J. M. C.; Bromley, S. T. Dust  
649 formation in the oxygen-rich AGB star IK Tauri. *Astron. Astrophys.* **2016**, 585, art. no.: A6.
- 650 (17). Álvarez-Barcia, S.; Flores, J. R. Can alumina particles be formed from Al hydroxide in  
651 the circumstellar media? A first-principles chemical study. *Phys. Chem. Chem. Phys.* **2016**,  
652 18, 6103-6112.
- 653 (18). Decin, L.; Justtanont, K.; De Beck, E.; Lombaert, R.; de Koter, A.; Waters, L. B. F. M.;  
654 Marston, A. P.; Teyssier, D.; Schöier, F. L.; Bujarrabal, V., et al. Water content and wind  
655 acceleration in the envelope around the oxygen-rich AGB star IK Tauri as seen by  
656 Herschel/HIFI. *Astron. Astrophys.* **2010**, 521, art. no.: L4.
- 657 (19). Frisch, M. J.; Trucks, G. W.; Schlegel, H. B.; Scuseria, G. E.; Robb, M. A.;  
658 Cheeseman, J. R.; Scalmani, G.; Barone, V.; Petersson, G. A.; Nakatsuji, H., et al. *Gaussian*  
659 *16, Revision B.01*, Gaussian, Inc.: Wallingford, CT, USA, 2016.
- 660 (20). Curtiss, L. A.; Redfern, P. C.; Raghavachari, K. Gaussian-4 theory. *J. Chem. Phys.*  
661 **2007**, 126, art. no.: 084108.
- 662 (21). Carrillo-Sánchez, J. D.; Gómez-Martín, J. C.; Bones, D. L.; Nesvorný, D.; Pokorný, P.;  
663 Benna, M.; Flynn, G. J.; Plane, J. M. C. Cosmic dust fluxes in the atmospheres of Earth,  
664 Mars, and Venus. *Icarus* **2020**, 335, art. no.: 113395.
- 665 (22). Plane, J. M. C.; Daly, S. M.; Feng, W. H.; Gerding, M.; Martin, J. C. G. Meteor-  
666 Ablated Aluminum in the Mesosphere-Lower Thermosphere. *J. Geophys. Res.-Space Phys.*  
667 **2021**, 126, art. no.: e2020JA028792.
- 668 (23). Gómez Martín, J. C.; Daly, S. M.; Brooke, J. S. A.; Plane, J. M. C. Absorption cross  
669 sections and kinetics of formation of AlO at 298K. *Chem. Phys. Lett.* **2017**, 675, 56-62.
- 670 (24). Plane, J. M. C.; Flynn, G. J.; Määttänen, A.; Moores, J. E.; Poppe, A. R.; Carrillo-  
671 Sanchez, J. D.; Listowski, C. Impacts of cosmic dust on planetary atmospheres and surfaces.  
672 *Space Sci. Rev.* **2017**, 214, art. no.: 23.
- 673 (25). Parnis, J. M.; Mitchell, S. A.; Kanigan, T. S.; Hackett, P. A. Gas-phase reactions of  
674 AlO with small molecules. *J. Phys. Chem.* **1989**, 93, 8045-8052.

- 675 (26). McClean, R. E.; Nelson, H. H.; Campbell, M. L. Kinetics of the reaction  $\text{Al}(^2\text{P})$  over  
676 an extended temperature range. *J. Phys. Chem.* **1993**, *97*, 9673-9676.
- 677 (27). Mangan, T. P.; McAdam, N.; Daly, S. M.; Plane, J. M. C. Kinetic Study of Ni and NiO  
678 Reactions Pertinent to the Earth's Upper Atmosphere. *J. Phys. Chem. A* **2019**, *123*, 601-610.
- 679 (28). Teghil, R.; Ferro, D.; Bencivenni, L.; Pelino, M. A thermodynamic study of the  
680 sublimation processes of aluminium and copper acetylacetonates. *Thermochimica Acta* **1981**,  
681 *44*, 213-222.
- 682 (29). Saksena, M. D.; Deo, M. N.; Sunanda, K.; Behere, S. H.; Londhe, C. T. Fourier  
683 transform spectral study of  $\text{B}^2\Sigma^+ - \text{X}^2\Sigma^+$  system of AlO. *J. Molec. Spectr.* **2008**, *247*, 47-56.
- 684 (30). Mangan, T. P.; Harman-Thomas, J. M.; Lade, R. E.; Douglas, K. M.; Plane, J. M. C.  
685 Kinetic Study of the Reactions of AlO and OAlO Relevant to Planetary Mesospheres. *ACS*  
686 *Earth Space Chem.* **2020**, *4*, 2007-2017.
- 687 (31). Gilbert, R. G.; Smith, S. C. *Theory of Unimolecular and Recombination Reactions*.  
688 Blackwell: Oxford, 1990.
- 689 (32). Mayer, S. W.; Schieler, L.; Johnston, H. S. Computation of high-temperature rate  
690 constants for bimolecular reactions of combustion products. *Symp. Int. Combust. Proc.* **1967**,  
691 *11*, 837 - 844.
- 692 (33). Sharipov, A.; Titova, N.; Starik, A. Kinetics of Al+H<sub>2</sub>O Reaction: Theoretical Study. *J.*  
693 *Phys. Chem. A* **2011**, *115*, 4476-4481.
- 694 (34). Álvarez-Barcia, S.; Flores, J. R. A theoretical study of the dynamics of the Al + H<sub>2</sub>O  
695 reaction in the gas-phase. *Chem. Phys.* **2011**, *382*, 92-97; Sun, Y.; Tian, Y.; Li, S. Theoretical  
696 Study on Reaction Mechanism of Aluminum-Water System. *Chin. J. Chem. Phys.* **2008**, *21*,  
697 245 - 249.
- 698 (35). Barnes, E. C.; Petersson, G. A.; Montgomery, J. A.; Frisch, M. J.; Martin, J. M. L.  
699 Unrestricted Coupled Cluster and Brueckner Doubles Variations of W1 Theory. *J. Chem.*  
700 *Theory Comput.* **2009**, *5*, 2687-2693.
- 701 (36). Glowacki, D. R.; Liang, C.-H.; Morley, C.; Pilling, M. J.; Robertson, S. H. MESMER:  
702 An Open-Source Master Equation Solver for Multi-Energy Well Reactions. *J. Phys. Chem. A*  
703 **2012**, *116*, 9545-9560.
- 704 (37). Rollason, R. J.; Plane, J. M. C. A Kinetic Study of the Reactions of MgO with H<sub>2</sub>O,  
705 CO<sub>2</sub> and O<sub>2</sub>: Implications for Magnesium Chemistry in the Mesosphere. *Phys. Chem. Chem.*  
706 *Phys.* **2001**, *3*, 4733-4740.
- 707 (38). Curtiss, L. A.; Redfern, P. C.; Raghavachari, K. Gaussian-4 theory. *J. Chem. Phys.*  
708 **2007**, *126*, art. no.: 084108.
- 709 (39). Feast, M. W. The pulsation, temperatures and metallicities of Mira and semiregular  
710 variables in different stellar systems. *Mon. Not. Roy. Astron. Soc.* **1996**, *278*, 11-21; Olofsson,  
711 H.; González Delgado, D.; Kerschbaum, F.; Schöier, F. L. Mass loss rates of a sample of  
712 irregular and semiregular M-type AGB-variables. *Astron. Astrophys.* **2002**, *391*, 1053-1067.

- 713 (40). Hindmarsh, A. C. LSODE and LSODI, two new initial value ordinary differential  
714 equation solvers. *ACM Signum Newsletter* **1980**, *15*, 10-11.
- 715 (41). Cristallo, S.; Straniero, O.; Piersanti, L.; Gobrecht, D. Evolution, nucleosynthesis, and  
716 yields of AGB stars at different metallicities. III. Intermediate-mass models, revised low-  
717 mass models, and the pH-FRUIITY interface. *Astrophys. J. Suppl. Ser.* **2015**, *219*, art. no.: 40.
- 718 (42). Höfner, S.; Olofsson, H. Mass loss of stars on the asymptotic giant branch:  
719 Mechanisms, models and measurements. *Astron. Astrophys. Rev.* **2018**, *26*, art. no.: 1.
- 720 (43). Manion, J. A.; Huie, R. E.; Levin, R. D.; D. R. Burgess Jr.; Orkin, V. L.; Tsang, W.;  
721 McGivern, W. S.; Hudgens, J. W.; Knyazev, V. D.; Atkinson, D. B., et al., NIST Chemical  
722 Kinetics Database, NIST Standard Reference Database 17, Version 7.0 (Web Version),  
723 Release 1.6.8, Data version 2015.09 National Institute of Standards and Technology:  
724 Gaithersburg, Maryland, 2021.
- 725 (44). Bauernschmitt, R.; Ahlrichs, R. Treatment of electronic excitations within the adiabatic  
726 approximation of time dependent density functional theory. *Chem. Phys. Lett.* **1996**, *256*,  
727 454-464.
- 728 (45). Gustafsson, B.; Edvardsson, B.; Eriksson, K.; Jørgensen, U. G.; Nordlund, Å.; Plez, B.  
729 A grid of MARCS model atmospheres for late-type stars. I. Methods and general properties.  
730 *Astron. Astrophys.* **2008**, *486*, 951-970.
- 731 (46). Trabelsi, T.; Francisco, J. S. Is AlOH the Astrochemical Reservoir Molecule of AlO?:  
732 Insights from Excited Electronic States. *Astrophys. J.* **2018**, *863*, art. no.: 139.
- 733 (47). Asplund, M.; Grevesse, N.; Sauval, A. J.; Scott, P. The Chemical Composition of the  
734 Sun *Ann. Rev. Astron. Astrophys.* **2009**, *47*, 481-522.
- 735 (48). Danilovich, T.; Gottlieb, C. A.; Decin, L.; Richards, A. M. S.; Lee, K. L. K.; Kamiński,  
736 T.; Patel, N. A.; Young, K. H.; Menten, K. M. Rotational Spectra of Vibrationally Excited  
737 AlO and TiO in Oxygen-rich Stars. *Astrophys. J.* **2020**, *904*, art. no.: 110.
- 738
- 739

740 For Table of Contents Only

741



742